Fabrication and characterization of MEMS-based PZT/PZT bimorph thick film vibration energy harvesters

2012 J. Micromech. Microeng. 22 094007

(http://iopscience.iop.org/0960-1317/22/9/094007)

J. Micromech. Microeng. **22** (2012) 094007 (9pp) doi:10.1088/0960-1317/22/9/094007

Fabrication and characterization of MEMS-based PZT/PZT bimorph thick film vibration energy harvesters

R Xu[1], A Lei[1], C Dahl-Petersen[1], K Hansen[2], M Guizzetti[2], K Birkelund[1], E V Thomsen[1] and O Hansen[1,3]

[1] Department of Micro- and Nanotechnology, Technical University of Denmark (DTU Nanotech), Building 345 East, DK-2800 Kongens Lyngby, Denmark
[2] Meggitt Sensing Systems, DK-3490 Kvistgaard, Denmark
[3] Center for Individual Nanoparticle Functionality (CINF), Technical University of Denmark, DK-2800 Kongens Lyngby, Denmark

E-mail: ruichao.xu@nanotech.dtu.dk

Received 25 January 2012, in final form 16 June 2012
Published 24 August 2012
Online at stacks.iop.org/JMM/22/094007

Abstract
We describe the fabrication and characterization of a significantly improved version of a microelectromechanical system-based PZT/PZT thick film bimorph vibration energy harvester with an integrated silicon proof mass; the harvester is fabricated in a fully monolithic process. The main advantage of bimorph vibration energy harvesters is that strain energy is not lost in mechanical support materials since only $Pb(Zr_xTi_{1-x})O_3$ (PZT) is strained; as a result, the effective system coupling coefficient is increased, and thus a potential for significantly higher output power is released. In addition, when the two layers are connected in series, the output voltage is increased, and as a result the relative power loss in the necessary rectifying circuit is reduced. We describe an improved process scheme for the energy harvester, which resulted in a robust fabrication process with a record high fabrication yield of 98%. The robust fabrication process allowed a high pressure treatment of the screen printed PZT thick films prior to sintering. The high pressure treatment improved the PZT thick film performance and increased the harvester power output to 37.1 μW at 1 g root mean square acceleration. We also characterize the harvester performance when only one of the PZT layers is used while the other is left open or short circuit.

(Some figures may appear in colour only in the online journal)

1. Introduction

Wireless monitoring and sensing systems have received significant attention in recent years, since they offer several advantages compared to their wired counterparts. In health care, for instance, a patient with a wireless monitoring system may still be mobile, while a wired monitoring system leaves the patient rather immobile. Some monitoring systems will be placed in remote areas where it is desirable that the system is wireless, a feature that will be equally desirable for the increasing number of portable complex electronic systems in use today. Conventionally, these systems are powered by batteries; however, the maintenance costs related to battery replacement can be quite significant. As a result, energy harvester solutions offering maintenance-free power supply of sensing or monitoring systems have attracted significant attention recently.

In the external surroundings, energy such as ambient light, mechanical vibrations, sound, or thermal gradients is available to be harvested for free. With the advances in micro-technology, many useful electronic systems have low enough power requirements to make completely self-supported systems realistic [1]. One of the methods to harvest mechanical energy from vibrations is to make use of the piezoelectric transduction mechanism [2]. A typical piezoelectric energy harvester is based on a cantilever beam,

which consists of the active piezoelectric ceramic with metal electrodes on both sides and a passive mechanical support structure, anchored at one end and with a proof mass at the other [3–6]. The main advantage of PZT/PZT thick film bimorph energy harvesters, compared to the aforementioned harvesters, is that strain energy is not lost in mechanical support materials since only PZT is strained, and thus it has a potential for higher power output. An additional advantage arises from a significantly increased output voltage of a series-connected bimorph harvester, which reduces the relative magnitude of the inevitable losses in rectifying support circuitry. Bulk PZT bimorph energy harvesters and models of these were presented in [7, 8], while a microelectromechanical system (MEMS)-sized bimorph energy harvester was recently introduced in [9]. Screen printed PZT thick film was used in [10], where multimorph energy harvesters were fabricated and characterized. We presented a first generation MEMS bimorph PZT/PZT thick film harvester in [11, 12], where it was shown that by using PZT thick film, it is possible to realize a self-supporting device without the need for a passive mechanical structure. However, the fabrication yield was low due to a process sequence with an early deep reactive ion etch (DRIE) step, which turned most of the structure into a fragile membrane. A revised process plan, using the advantageous process steps introduced in [13], has significantly improved both fabrication yield and performance of the harvesters. The DRIE step was replaced by a potassium hydroxide (KOH) wet etch and moved to the last part of the fabrication process; as a result, the fabrication yield was more than triple to a record high yield of 98.6%. As an added benefit, the improved mechanical stability of the structure during PZT thick film (InSensor® TF2100) deposition and processing allowed high pressure treatment of the PZT thick film before sintering; this resulted in more than a fivefold improvement of the harvester power output compared to previous results [11]. Furthermore, the use of KOH etching may facilitate a scalable future mass production.

2. Fabrication

The fabricated energy harvester, shown in figure 1, combines PZT thick film screen printing with standard MEMS technology into a monolithic fabrication process. The harvester comprises a 10 mm × 10 mm silicon frame fitted with a wide PZT/PZT bimorph cantilever beam with bottom, top and middle electrodes. At the free end of the cantilever beam, a silicon proof mass is fixed. Contacts to the three electrodes are placed on the silicon frame.

In the design of the fabrication process, the main emphasis was on ensuring high mechanical stability of the wafers until completion the PZT/PZT stack by postponing bulk silicon structuring; this was accomplished by the use of KOH etching of silicon just prior to the release of the cantilever beams. As a result, high pressure treatment of the thick film PZT layers prior to sintering became feasible. This significantly improved the quality of the PZT material and the fabrication yield. The electrode materials for the PZT/PZT stack were chosen for compatibility with the PZT sintering process (∼850 °C); in this process, the bottom metal layer has to serve also as a diffusion barrier to prevent diffusion of silicon into the PZT layers, since silicon contamination ruins the piezoelectric material. For this reason, Pt was chosen for both the bottom electrode and the middle electrode, while for the top electrode, which is not sintered, Au was the material of choice since it does not oxidize readily.

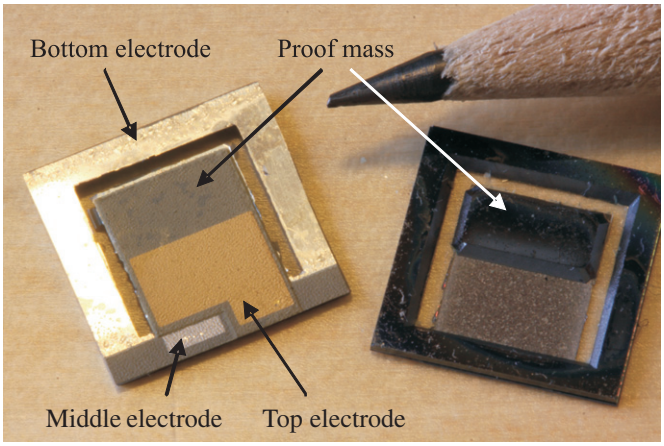

Figure 1. Photographic image showing the front and back of the 10 mm × 10 mm energy harvesters.

The fabrication process is illustrated in figure 2. The fabrication process starts with a double-sided polished 4 inch (100 mm) silicon on insulator (SOI) wafer with a 20 μm device layer and 1 μm buried oxide on a 525 μm handle substrate, as shown in figure 2(*a*). First, a 1 μm thick silicon dioxide is thermally grown at 1150 °C, and then a 170 nm thick silicon nitride is deposited using low pressure chemical vapor deposition (LPCVD), as shown in figure 2(*b*). The nitride is removed on the front side using reactive ion etch (RIE), and after that the back side of the wafer is patterned using conventional lithography processes and similarly etched in RIE, as shown in figure 2(*c*). Next, a 50 nm titanium (Ti) adhesion layer and a 500 nm platinum (Pt) bottom electrode are deposited using e-beam evaporation on the front side of the wafer, which is subsequently patterned using AZ4562 resist, followed by an etch in a wet etch solution, H_2O:HCl:HNO_3 (8:7:1) at 85 °C for 8 min, as shown in figure 2(*d*). Thereafter, the PZT thick film layer is screen printed on the patterned bottom electrode, high pressure treated [14] and sintered; here the bottom electrode also serves as a diffusion barrier. The advantage of using the new fabrication scheme appears here: screen printing and high pressure treatment of the PZT layer is done on a full wafer, instead of a wafer with thin membranes as it was done in [11, 12]; this not only prevents any chip loss during PZT processing but also ensures a higher quality and more uniform thick film that will prevent any cantilever breakage after the final release etch. Next, the 500 nm Pt middle electrode is deposited through a prefabricated silicon shadow mask using e-beam evaporation, as shown in figure 2(*e*). The shadow mask was made using a 350 μm thick silicon wafer, which was patterned using UV lithography and etched through in a DRIE process. The second PZT thick film layer is then screen printed, high pressure treated and sintered. This is followed by the deposition of a 500 nm gold (Au)

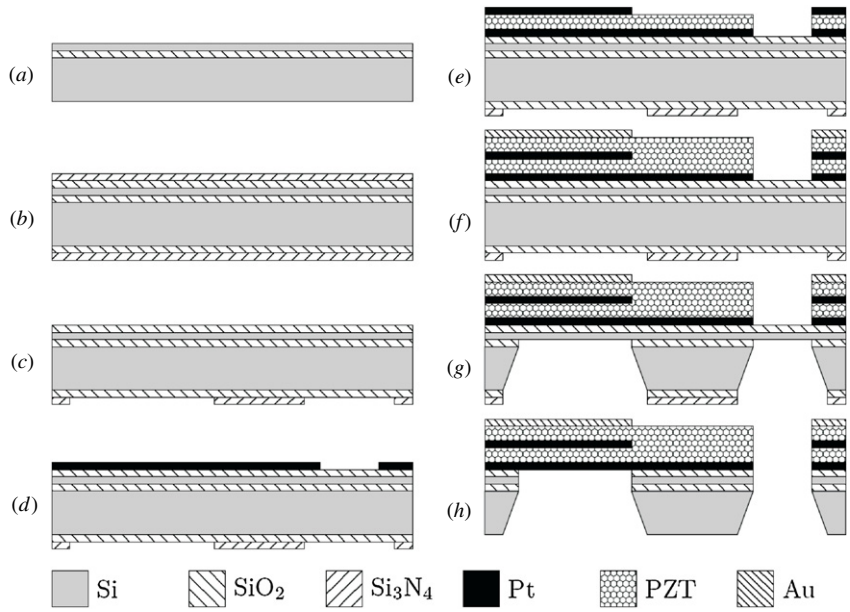

Figure 2. Cross-sectional view of the fabrication scheme. First, a 1 μm thick silicon dioxide is thermally grown on a SOI wafer (*a*), and then a 170 nm thick silicon nitride is deposited using LPCVD (*b*). The nitride is removed on the front side and patterned on the back side using conventional lithography processes (*c*). A Pt bottom electrode is deposited on the front side of the wafer and patterned (*d*), followed by deposition of the first PZT thick film layer, the Pt middle electrode (*e*), the second PZT thick film layer and the Au top electrode (*f*). The oxide on the back side is etched in bHF, while the front side of the SOI wafer is protected. The back side of the SOI wafer is then etched in KOH until the buried oxide layer is reached and then the buried oxide layer is removed in bHF (*g*). Finally, the sacrificial device layer is etched in RIE, releasing the cantilevers (*h*).

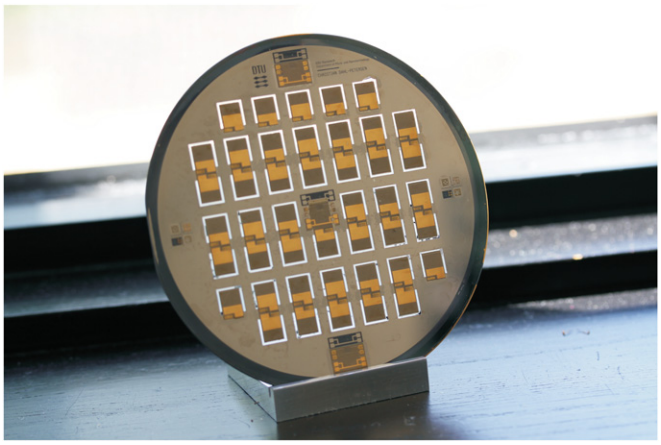

Figure 3. Image of a fabricated harvester wafer before dicing.

top electrode through another prefabricated shadow mask, fabricated using the aforementioned fabrication steps; see figure 2(*f*). Thereafter, the wafer is mounted on a 4 inch tandem series wafer holder from advanced micromachining tools. The oxide on the back side is etched in buffered hydrofluoric acid (bHF), while the front side of the SOI wafer is protected by the holder. Then, the silicon is etched in a KOH etch until the buried oxide layer is reached and then the buried oxide layer is removed in bHF, as shown in figure 2(*g*). Finally, the sacrificial device layer is etched in RIE, releasing the cantilevers; see figure 2(*h*).

Figure 3 shows the fabricated harvester wafer before dicing. Note that all cantilevers are intact; the chip yield on the wafer at this stage is still 100%, while if the fabrication process from [11, 12] was used, the chip yield would be much less.

Table 1. Energy harvester dimensions.

Frame dimensions	10 mm × 10 mm
Medial dimensions	< 1 mm
Cantilever width	5.5 mm
Cantilever length	3.25 mm
Total cantilever height	2 × 20 μm
Proof mass length	3.25 mm
Mass of the proof mass	25 mg

The wafer is diced and the chips are polarized individually. The polarization directions of the two layers are aligned opposite to each other, i.e. during polarization the top and bottom electrodes are grounded and a polarization voltage is applied to the middle electrode. The dimensions for the final energy harvester chips are shown in table 1.

In figure 4 a scanning electron microscope (SEM) image of a cross-section of the PZT/PZT bimorph cantilever beam resulting from this fabrication process is shown. The two PZT layers are seen to be similar both with respect to thickness and morphology, and they have a rather low porosity as a result of the high pressure treatment prior to sintering.

3. Theory

The PZT/PZT bimorph beam energy harvester is really a distributed system and full distributed models have been derived [8], but since the harvester is operated near the first resonant frequency, a lumped model of the system is sufficiently accurate [7]. Here we will develop such a

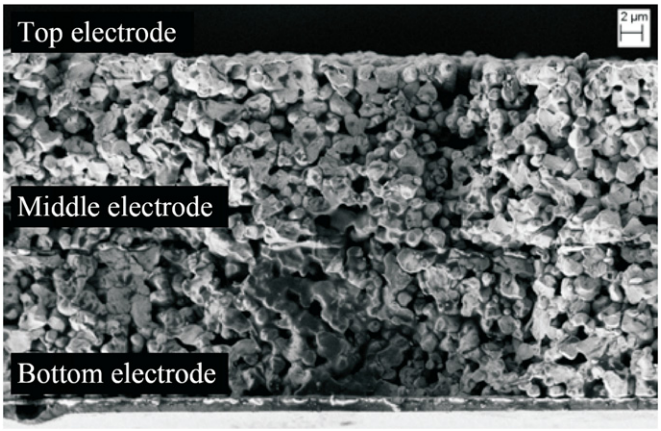

Figure 4. SEM image showing a cross-sectional view of the PZT/PZT bimorph thick film structure. The thin top, middle and bottom electrodes are barely visible in this magnification.

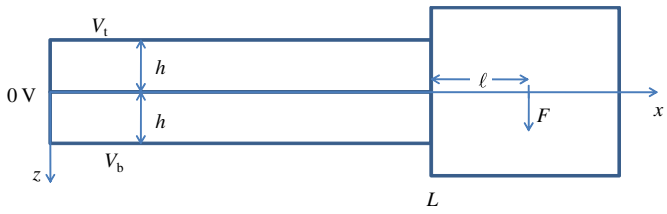

Figure 5. Schematic cross-section of the bimorph energy harvester. The bimorph PZT beam consists of two PZT layers, which are assumed to have the thickness h. At $x = 0$ the beam is rigidly clamped to a frame, and at $x = L$ a proof mass (of mass m) is fixed to the beam. The center of gravity for the proof mass is at $x = L + \ell$, where $\ell = L_m/2$ is half of the length of the proof mass.

lumped model based on a bimorph piezoelectric beam model, derived from the constitutive piezoelectric materials equations [15, 16], and a solution to Euler's beam equation. We shall consider a symmetric piezoelectric bimorph beam where each layer has the thickness h, length L and width W. On the beam, top and bottom electrodes covering the full top and bottom surfaces are assumed to be thin enough that their contribution to the beam stiffness may be ignored; likewise, the middle electrode that separates the two PZT layers is assumed infinitely thin. The potentials on the top, bottom and middle electrodes are V_t, V_b, and 0 V, respectively. The beam is clamped to a rigid frame in one end and has an attached proof mass of mass m on the other end; the center of gravity for the proof mass is positioned at the distance ℓ from the end of the beam, as illustrated in figure 5.

In the appendix, we show the that the harvester may be reasonably well described by a lumped element model comprising a force balance equation evaluated at the center of mass for the proof mass including forces from the voltages on the top and bottom electrodes

$$Z_m v_c = F + \frac{\Gamma_b}{\Lambda} V_b + \frac{\Gamma_t}{\Lambda} V_t, \tag{1}$$

combined with two equations for the currents I_t and I_b flowing into the top and bottom electrodes, respectively,

$$I_t = \frac{\Gamma_t}{\Lambda} v_c + sC_t V_t, \tag{2}$$

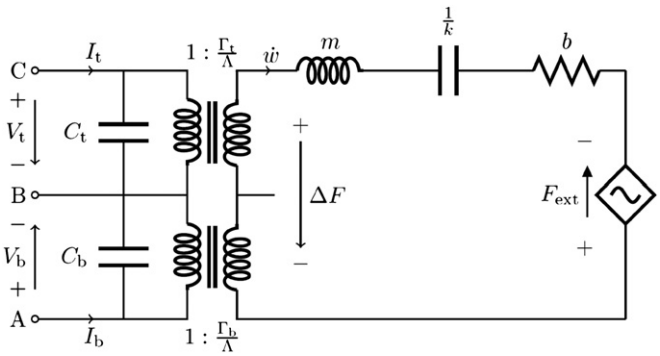

Figure 6. Equivalent circuit diagram for the bimorph PZT/PZT energy harvester.

$$I_b = \frac{\Gamma_b}{\Lambda} v_c + sC_b V_b, \tag{3}$$

where F is the external force acting on the proof mass, v_c is the velocity of the proof mass, $Z_m = sm + b + k/s$ is the mechanical impedance of the proof mass–spring system and $s = j\omega$ is the complex frequency. The proof mass has the mass m, k is the effective spring constant of the cantilever beam as seen from the proof mass, b is the loss coefficient for the mass–spring system and C_t and C_b are the total capacitances including parasitics of the top and bottom layers, respectively. Γ_t/Λ and Γ_b/Λ are transduction coefficients from velocity to current and from voltage to force for the top and bottom layers, respectively.

Equations (1)–(3) may be used to predict the behavior of the energy harvester when connected to external loads or under open circuit conditions, and the equations may be represented by the equivalent circuit diagram (figure 6).

The PZT/PZT bimorph energy harvester may be connected to external loads in several ways; one active layer may be used while the other is left open (1o) or short circuit (1s) or both layers may be used in parallel (2P) or in series (2S).

3.1. Single layer connected (1s)

The 1s situation essentially corresponds to a simple single PZT layer harvester, and may thus serve as a performance reference. This situation is easily analyzed, since e.g. $V_b = 0$, and $I_t = -G_L V_t$, where G_L is the load conductance, if the top layer is taken as the active layer. The output voltage V_t is then easily calculated

$$V_t = -F \frac{(\Gamma_t/\Lambda)}{(\Gamma_t/\Lambda)^2 + (sC_t + G_L)Z_m}, \tag{4}$$

while the input admittance of the harvester is

$$Y_{in_t} = \left(\frac{\Gamma_t}{\Lambda}\right)^2 \frac{1}{Z_m} + sC_t. \tag{5}$$

The resonant frequency becomes the native mechanical resonant frequency $\omega_r = \omega_0 = \sqrt{k/m}$, while the anti-resonant frequency is $\omega_a = \omega_0\sqrt{1 + K_t^2}$, where $K_t^2 = (\Gamma_t/\Lambda)^2/(kC_t)$ is the square of the system coupling coefficient for the top layer.

The output power is maximized at frequencies close to the anti-resonant frequency ω_a, and is approximately

$$P_{\max_t} = \frac{|F|^2_{\rm RMS}}{4b}\frac{2}{1+\sqrt{1+\frac{1+K_t^2}{Q^2K_t^4}}} = \frac{ma^2Q}{4\omega_0}\frac{2}{1+\sqrt{1+\frac{1+K_t^2}{Q^2K_t^4}}}, \tag{6}$$

where the first term is the available power. Here we have used that $|F|_{\rm RMS} = ma$ where a is the root mean square (RMS) acceleration amplitude of the external vibration, and that $b = m\omega_0/Q$ where Q is the mechanical quality factor. This power is obtained at an optimal load conductance of

$$G_{L\mathrm{opt}_t} = \frac{\omega_0 C_t\left(1+K_t^2\right)}{\sqrt{\left(1+K_t^2+Q^2K_t^4\right)}} = \frac{\omega_a C_t\sqrt{1+K_t^2}}{\sqrt{\left(1+K_t^2+Q^2K_t^4\right)}}. \tag{7}$$

3.2. Single connected layer (1o)

In the situation with one connected layer while the other is left open (1o), $I_b = 0$ and $I_t = -G_L V_t$ if the top layer is loaded. Solving equations (1)–(3) for the output voltage V_t yields

$$V_t = -F_{\rm ext}\frac{(\Gamma_t/\Lambda)}{(\Gamma_t/\Lambda)^2+\left(Z_m+(\Gamma_b/\Lambda)^2\frac{1}{sC_b}\right)\left(sC_t+G_L\right)}, \tag{8}$$

where it may be recognized that the open bottom layer causes an increase in the apparent spring constant such that the effective spring constant becomes $k + (\Gamma_b/\Lambda)^2/C_b$. This is also apparent in the input admittance

$$Y_{\mathrm{in}_t} = \frac{(\Gamma_t/\Lambda)^2}{\left(Z_m+(\Gamma_b/\Lambda)^2\frac{1}{sC_b}\right)} + sC_t. \tag{9}$$

As a result of the increased effective spring constant, the resonant frequency is larger than the native mechanical resonant frequency $\omega_r = \omega_0\sqrt{1+K_b^2}$ where $K_b^2 = (\Gamma_b/\Lambda)^2/(kC_b)$ is the coupling coefficient of the bottom layer. The anti-resonant frequency becomes $\omega_a = \omega_0\sqrt{1+K_b^2+K_t^2}$ as may easily be verified by inspection of the admittance.

The output power is maximized at frequencies near the anti-resonant frequency ω_a

$$P_{\max}(\omega_r) = \frac{|F|^2_{\rm RMS}}{4b}\frac{2}{1+\sqrt{1+\left(1+K_b^2+K_t^2\right)/\left(K_t^4Q^2\right)}}; \tag{10}$$

the output power is slightly smaller than the output power with the bottom layer short circuited due to the additional term K_b^2 and possibly due to a frequency-dependent quality factore.g. for thermo-mechanical losses, $Q\omega$ is approximately constant at low frequencies [17]). The power is maximized at the load conductance

$$G_{L\mathrm{opt}_t} = \frac{\omega_0 C_t\left(1+K_b^2+K_t^2\right)}{\sqrt{1+K_b^2+K_t^2+K_t^4Q^2}} = \frac{\omega_a C_t\sqrt{\left(1+K_b^2+K_t^2\right)}}{\sqrt{1+K_b^2+K_t^2+K_t^4Q^2}}. \tag{11}$$

3.3. Two loaded layers in parallel (2P)

When the two PZT layers are operated in parallel, the output voltage $V_{\rm out} = V_t = V_b$ and $I = I_t + I_b = -G_L V_{\rm out}$ and as a result equations (1)–(3) simplify to

$$Z_m v_c = F + (\Gamma_b/\Lambda + \Gamma_t/\Lambda)V_{\rm out}, \tag{12}$$

$$-G_L V_{\rm out} = (\Gamma_b/\Lambda + \Gamma_t/\Lambda)v_c + s(C_t+C_b)V_{\rm out}. \tag{13}$$

It follows that mathematically, the situation is exactly the same as in 1s, except for the increased capacitance and increased transduction coefficient. Note, in this configuration the two layers should be poled in the same direction to ensure that Γ_b and Γ_t have the same sign. The system coupling coefficient is in this case obtained from $K_p^2 = (\Gamma_b/\Lambda+\Gamma_t/\Lambda)^2/[k\,(C_t+C_b)]$. If the two layers are assumed identical $\Gamma_b = \Gamma_t = \Gamma_0$ and $C_t = C_b = C_0$, we see that as a result of the parallel layers the system coupling coefficient is increased to $K_p^2 = 2(\Gamma_0/\Lambda)^2/(kC_0)$, and as a result more power is harvested.

3.4. Two layers loaded in series

When the two PZT layers are loaded in series with a single load conductance $I_t = -I_b = -G_L V_{\rm out} = -G_L\,(V_t - V_b)$, and with these conditions equations (1)–(3) may be solved for $V_{\rm out}$ after tedious, but simple calculations, we shall not reproduce the result here, but rather consider only the much simpler situation where the two layers are identical but poled in opposite directions, and thus $V_t = -V_b = V_{\rm out}/2$. Then we may simplify equations (1)–(3) to

$$Z_m v_c = F + \frac{1}{2}\left(\frac{\Gamma_t}{\Lambda}-\frac{\Gamma_b}{\Lambda}\right)V_{\rm out}, \tag{14}$$

$$I_t = \frac{1}{2}\left(\frac{\Gamma_t}{\Lambda}-\frac{\Gamma_b}{\Lambda}\right)v_c + s\frac{C_t+C_b}{4}V_{\rm out}. \tag{15}$$

Mathematically, the situation is again identical to the 1s case, but the system coupling coefficient K_s is increased such that $K_s^2 = (\Gamma_t/\Lambda-\Gamma_b/\Lambda)^2/[k\,(C_t+C_b)] = 2\,(\Gamma_0/\Lambda)^2/(kC_0) = 2K_0^2$. With the perfect symmetry, the resonant frequency equals the native mechanical resonant frequency and the anti-resonant frequency becomes $\omega_a = \omega_0\sqrt{1+K_s^2}$. The output power is maximized near the anti-resonant frequency, and may be obtained by substitution into the equation for the 1s case, but we shall write it in full

$$P_{\max_s} = \frac{|F|^2_{\rm RMS}}{4b}\frac{2}{1+\sqrt{1+\frac{1+K_s^2}{Q^2K_s^4}}} = \frac{|F|^2_{\rm RMS}}{4b}\frac{2}{1+\sqrt{1+\frac{1+2K_0^2}{Q^24K_0^4}}}. \tag{16}$$

In devices where the product $K_0^{-4}Q^{-2}$ is relatively large (low coupling coefficient and moderate Q) the improvement in output power is significant. The optimal load conductance becomes

$$G_{L\mathrm{opt}_s} = \frac{\frac{1}{2}\omega_0 C_0\left(1+K_s^2\right)}{\sqrt{\left(1+K_s^2+Q^2K_s^4\right)}} = \frac{\frac{1}{2}\omega_0 C_0\left(1+2K_0^2\right)}{\sqrt{\left(1+2K_0^2+Q^24K_0^4\right)}}, \tag{17}$$

which is different from half of the optimal load conductance ($\omega_0 C_0 \frac{1+2K_0^2}{\sqrt{(1+2K_0^2+Q^2K_0^4)}}$) of the individual layers in an open circuit, or in other words, the optimal load resistance differs from the sum of optimal load resistances for the individual layers.

The output voltage becomes

$$V_{\text{out}} = -F \frac{(\Gamma_0/\Lambda)}{(\Gamma_0/\Lambda)^2 + \left(s\frac{C_0}{2} + G_L\right)Z_m}, \tag{18}$$

and especially at low coupling coefficients K_0 for the individual layers, the output voltage is significantly increased by series connection of the two layers. This is significant since the relative magnitude of rectifier losses is then reduced.

In addition, a detailed study of the power as a function of frequency shows that the bandwidth of the output power peak is increased when the system coupling coefficient is increased at fixed mechanical Q; this effect is most significant at rather low coupling coefficients for the individual layers. This is also true for the parallel-connected layers, which with respect to output power and bandwidth improvements performs equal to the series-connected layers. The two double-layer structures only differ (for symmetrical layers) with respect to the output voltage level and optimal load conductance, where the series-connected structure outperforms the parallel-connected structure due to the higher output voltage.

4. Results

The fabricated energy harvesters were characterized in a shaker setup, where a B&K Mini Shaker 4810 driven by an amplified sinusoidal signal from an Agilent 33220A function generator was used to simulate an external vibration from the environment. Both the energy harvester and a B&K Piezoelectric Accelerometer 8305 were mounted on the Mini Shaker. The accelerometer served as a reference for the input RMS acceleration a, and measurements are reported in fractions of the gravitational acceleration g (9.81 m s^{-2}). The RMS power output is found by connecting the harvester to a resistive load while the voltage drop across the load was measured. The optimal resistive load, R_{opt}, was found by varying the resistive load in steps of 10 kΩ to achieve maximum dissipated power in the load resistance, i.e. $P_{\text{RMS}} = V_{\text{RMS}}^2/R_{\text{opt}}$. Figure 7 shows the power output of the harvester as a function of the frequency for different input accelerations, measured with the PZT layers connected in series, i.e. the load is connected between bottom and top electrodes. The optimal resistive load used here was R_{opt}=200 kΩ. At 1 g input acceleration, the power output reaches 37.1 μW.

The output power from the bottom PZT layer and the top PZT layer was measured using the same measurement scheme. During measurements on the top PZT layer, the top and middle electrodes were connected to the load, while the bottom electrode was left open circuit. The optimal resistive load was found to be 130 kΩ for the top layer. Similarly, during measurements on the bottom PZT layer, the bottom and middle electrodes were connected to the load and the top electrode was left open circuit. The optimal resistive load was found to be 90 kΩ for the bottom layer. The peak output power from the

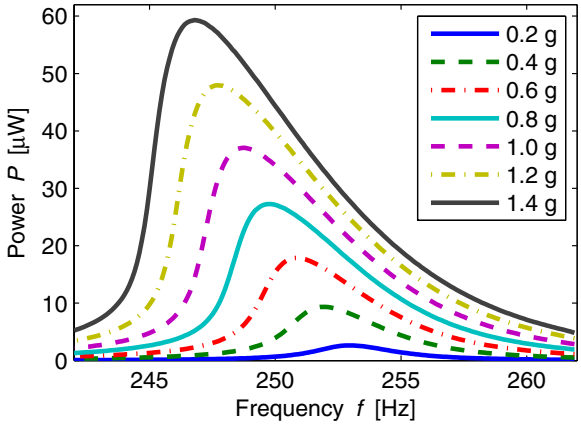

Figure 7. RMS power output of both PZT layers combined as a function of frequency near the resonant frequency for different RMS input accelerations at an optimal resistive load of 200 kΩ.

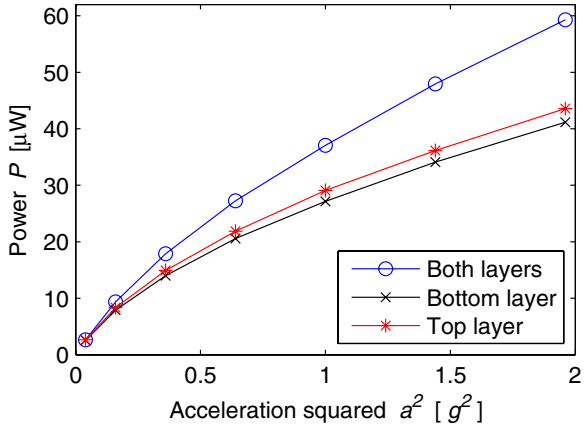

Figure 8. RMS power output from the top PZT layer, the bottom PZT layer and both layers combined as a function of the RMS input acceleration squared a^2 at their respective optimal resistive loads.

measurements yields the plot reported in figure 8, where the output power in the three cases (top layer, bottom layer and both layers connected to the load) is shown as a function of the input acceleration squared. The bandwidth, defined as the full-width at half-maximum of the data such as those in figure 7, was extracted for all measurements and is reported in figure 9.

4.1. Short versus open circuit

In measurements of the output power from the individual PZT layers, e.g. the bottom PZT layer, the top electrode may either be left open circuit as was done above or short circuited to the middle electrode. In figures 10 and 11, we compare the RMS output power from the top and bottom layers, respectively, when the third electrode is left open or short circuit.

Figures 10 and 11 both show an increase in the peak power frequency in the case of the open circuit configuration compared to that of the short circuit configuration. This is expected as shown in section 3. The shift is slightly larger for the bottom PZT layer than for the top PZT layer; the reason is that the top layer has a slightly larger system coupling coefficient than the bottom layer (partly due to a larger parasitic

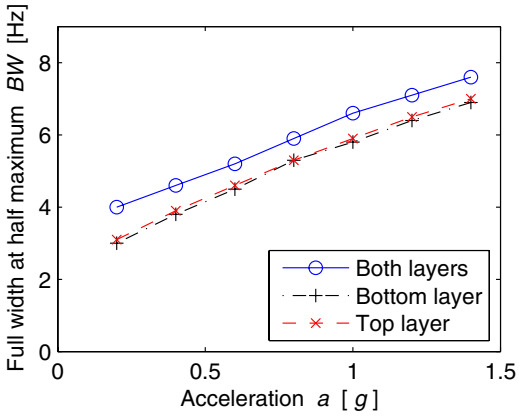

Figure 9. The full-width at half-maximum bandwidth for the top PZT layer, the bottom PZT layer and both layers combined as a function of the RMS input acceleration at their respective optimal resistive loads.

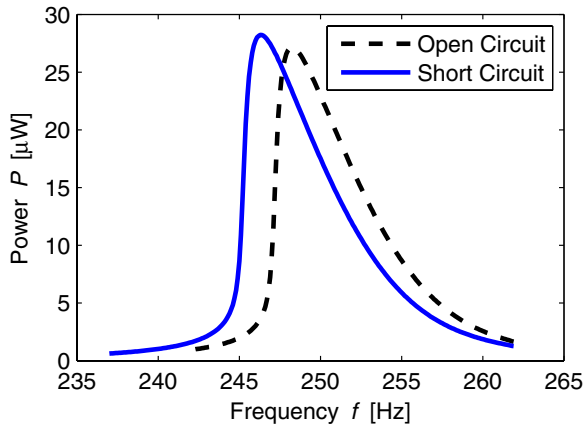

Figure 10. RMS power output of the bottom PZT layer as a function of frequency near the resonant frequency at 1 *g* RMS input acceleration where the top electrode is open or short circuit with respect to the middle electrode.

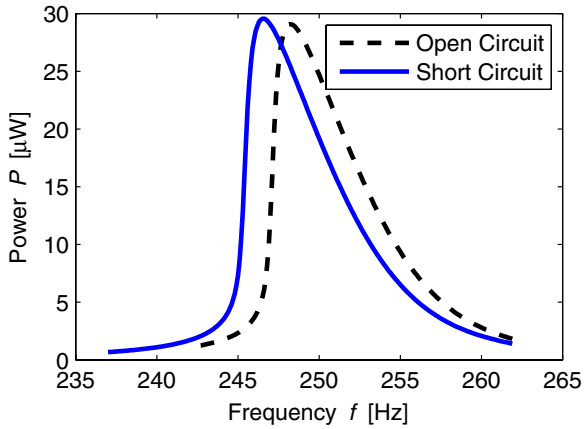

Figure 11. RMS power output of the top PZT layer as a function of frequency near the resonant frequency at 1 *g* RMS input acceleration where the bottom electrode is open or short circuit with respect to the middle electrode.

capacitance of the bottom PZT layer), and the shift in peak power frequency for the bottom layer is due to added effective spring constant from the top layer as shown in section 3.

Table 2. The relative change in the output power $(P_{sc} - P_{oc})/P_{oc}$ and peak power frequency shift $\Delta f_0 = f_{0oc} - f_{0sc}$ when short circuit configuration measurements are compared to open circuit configuration measurements during characterization of the individual layers.

RMS acceleration a (g)	0.6	0.8	1.0	1.2	1.4
$(P_{sc} - P_{oc})/P_{oc}$ (%)					
Bottom layer	3.06	2.92	3.94	4.40	4.98
Top layer	0.51	1.83	1.67	3.11	4.03
$f_{0oc} - f_{0sc}$ (Hz)					
Bottom layer	1.9	1.9	2.0	2.0	1.9
Top layer	1.7	1.7	1.6	1.7	1.7

Explicitly, we expect that $f_{0oc_b}^2 - f_{0sc_b}^2 = f_0^2 K_t^2$, where f_{0oc_b} and f_{0sc_b} are the peak frequencies in open and short circuit conditions, respectively, and f_0 is the mechanical resonance frequency. The slightly lower output power from the bottom layer compared to the top layer is caused by the slightly lower coupling coefficient for the bottom layer compared to that of the top layer.

Another trend is that the short circuit configuration generates slightly higher output power than that of the open circuit configuration. This is also expected as shown in section 3. Table 2 shows the relative change in output power $(P_{sc} - P_{oc})/P_{oc}$ and the shift in peak power frequency $\Delta f_0 = f_{0oc} - f_{0sc}$ when the short circuit (subscript sc) configuration measurements are compared to the open circuit (subscript oc) configuration measurements of the individual layers.

5. Discussion

The resonant frequency shift as a function of the acceleration observed in figure 7 was also seen in [11, 12], where it was explained to be caused by a nonlinear softening effect. Even though such an effect is still present in the pressure treated harvester, the softening effect is much less prominent compared to that in [11]. As a result, the resonant frequency shift with acceleration is smaller, and the frequency responses become more symmetrical around the resonance peaks. From figure 8 it can be noted that the power outputs of the two individual layers are almost identical; this was not the case in [11, 12]. Apparently, the use of high pressure treatments renders the two PZT thick film layers quite similar. This is supported by the SEM inspection shown in figure 4, where a cross-sectional view of the cantilever shows that the two layers are very similar both in thickness and morphology which was not the case in a similar study in [11]. The difference in the optimal resistive loads with such similar films is partly due to a larger parasitic capacitance and thus a larger total capacitance of the bottom layer compared to the top layer caused by layout differences. The output power from both layers combined in series is as expected higher than the output power from the individual layers due to the increased system coupling coefficient, but significantly less than the sum of the powers from the two individual layers. The increased system coupling coefficient also improves the useful bandwidth as shown in figure 9 where the bandwidth of both layers combined in series is about 1 Hz larger than that of each layer for all input

accelerations. As a result, the output power and the useful bandwidth are both increased by the use of two PZT layers, and the harvester becomes useful in a wider spectrum of vibrations. The measured RMS power output at 1 g acceleration is 37.1 μW, which is comparable to the best performing MEMS energy harvesters reported in the literature in recent years [6, 18].

6. Conclusion

MEMS-based PZT/PZT bimorph thick film vibration energy harvesters were successfully fabricated and characterized. By implementing an improved fabrication process, a fabrication yield of 98.6% was achieved. The revised process plan made high pressure treatment of the PZT thick film layers before sintering feasible. As a result, the two PZT layers became denser and more similar in thickness and morphology. The power outputs at 1 g for the top and bottom layers were 29.1 and 27.2 μW, respectively. The power output with both layers combined was 37.1 μW at 1 g with a bandwidth value of 7 Hz.

Acknowledgments

This research is part of the ELBA project, which is funded by the Advanced Technology Foundation. Center for Individual Nanoparticle Functionality (CINF) is sponsored by the Danish National Research Foundation.

Appendix

The starting point for the piezoelectric beam model is the constitutive piezoelectric material equations [16]. Since both the electric field **E** (due to the electrodes) and the stress **T** (due to pure bending) are unidirectional, the simplest material relations are obtained if electric displacement **D** and strain **S** are expressed as functions of the non-zero electric field E_3 and the stress T_1, and then the simplified material relations [16]

$$S_1 = s_{11}T_1 + \mathrm{d}_{31}E_3, \tag{A.1}$$

$$D_3 = d_{31}T_1 + \varepsilon_{33}E_3, \tag{A.2}$$

result, where only three material parameters, the compliance s_{11}, the piezoelectric coefficient d_{31} and the permittivity ε_{33}, are needed. Ideally, these parameters should have superscripts T or E to indicate that they are material parameters at constant stress or electric field, but in the interest of a simple notation the superscripts are omitted. The beam is subject to pure bending and thus the geometrical strain $S_1 = -zw''_{xx}$ results, where w is the beam deflection, while z is the position relative to the neutral axis of the beam. We shall ignore longitudinal beam displacement u.

Since the strain is known, it is useful to rearrange equations (A.1) and (A.2) to yield

$$T_1 = \frac{1}{s_{11}}S_1 - \frac{\mathrm{d}_{31}}{s_{11}}E_3, \tag{A.3}$$

$$D_3 = \frac{\mathrm{d}_{31}}{s_{11}}S_1 + \varepsilon_{33}\left(1 - \frac{\mathrm{d}_{31}^2}{s_{11}\varepsilon_{33}}\right)E_3 = \frac{\mathrm{d}_{31}}{s_{11}}S_1 + \varepsilon_{33}\left(1 - k_{31}^2\right)E_3, \tag{A.4}$$

where $k_{31} = \sqrt{d_{31}^2/(s_{11}\varepsilon_{33})}$ is the piezoelectric coupling coefficient. The currents flowing into the top ($I_{\mathrm{t}0}$) and bottom electrodes ($I_{\mathrm{b}0}$) may be calculated from integrals of equation (A.4) over the volumes of the individual layers using the space charge free condition ($\nabla \cdot \mathbf{D} = 0$) and the beam boundary conditions ($w(0) = 0$, and $w'_x(0) = 0$)

$$I_{\mathrm{t}0} = \dot{Q}_{\mathrm{t}0} = \frac{\mathrm{d}_{31\mathrm{t}}}{s_{11}}\frac{Wh_{\mathrm{t}}}{2}\dot{w}'_x(L) + \frac{\varepsilon_{33}\left(1 - k_{31\mathrm{t}}^2\right)WL}{h_{\mathrm{t}}}\dot{V}_{\mathrm{t}}, \tag{A.5}$$

$$I_{\mathrm{b}0} = \dot{Q}_{\mathrm{b}0} = \frac{\mathrm{d}_{31\mathrm{b}}}{s_{11}}\frac{Wh_{\mathrm{b}}}{2}\dot{w}'_x(L) + \frac{\varepsilon_{33}\left(1 - k_{31\mathrm{b}}^2\right)WL}{h_{\mathrm{b}}}\dot{V}_{\mathrm{b}}, \tag{A.6}$$

where $\dot{X}$ is a shorthand for $\partial X/\partial t$. Here subscripts t and b are used on material parameters to allow for e.g. different poling directions of the layers; in addition, subscript is also added to the layer thicknesses even though they are assumed identical. The currents are seen to depend on the slope rate $\dot{w}'_x(L)$ at the end of the beam, but that is identical to the slope rate of the proof mass and from the solution to Euler's beam equation, the slope and center of gravity deflection of the proof mass w_c are related by $w_c = \Lambda w'_x(L)$, with $\Lambda = 2\left(L^2 + 3L\ell + 3\ell^2\right)/\left[3\left(L + 2\ell\right)\right]$.

In addition to the capacitances $C_{\mathrm{t}0} = \varepsilon_{33}\left(1 - k_{31\mathrm{t}}^2\right)WL/h_{\mathrm{t}}$ and $C_{\mathrm{b}0} = \varepsilon_{33}\left(1 - k_{31\mathrm{b}}^2\right)WL/h_{\mathrm{b}}$ of the active piezoelectric layers additional parasitic capacitances, $C_{\mathrm{t}p}$ and $C_{\mathrm{b}p}$ may be present on the electrodes due to e.g. contact pads. As a result, the total currents I_{t} and I_{b} to the electrodes may be expressed as follows:

$$I_{\mathrm{t}} = \frac{\Gamma_{\mathrm{t}}}{\Lambda}\dot{w}_c + C_{\mathrm{t}}\dot{V}_{\mathrm{t}}, \tag{A.7}$$

$$I_{\mathrm{b}} = \frac{\Gamma_{\mathrm{b}}}{\Lambda}\dot{w}_c + C_{\mathrm{b}}\dot{V}_{\mathrm{b}}, \tag{A.8}$$

with the coupling coefficients $\Gamma_{\mathrm{t}} = (d_{31\mathrm{t}}Wh_{\mathrm{t}})/(2s_{11})$ and $\Gamma_{\mathrm{b}} = (d_{31\mathrm{b}}Wh_{\mathrm{b}})/(2s_{11})$, and total capacitances $C_{\mathrm{t}} = C_{\mathrm{t}0} + C_{\mathrm{t}p}$ and $C_{\mathrm{b}} = C_{\mathrm{b}0} + C_{\mathrm{b}p}$.

The bending moment is the moment of stress T_1 around the y-axis, and is thus obtained from an integral of equation (A.3)

$$M = -w''_{xx}\int \frac{W}{s_{11}}z^2\,\mathrm{d}z + \frac{d_{31\mathrm{b}}}{s_{11}}\frac{Wh_{\mathrm{b}}}{2}V_{\mathrm{b}} + \frac{\mathrm{d}_{31\mathrm{t}}}{s_{11}}\frac{Wh_{\mathrm{t}}}{2}V_{\mathrm{t}}, \tag{A.9}$$

and thus we may write the total bending moment

$$M = -YIw''_{xx} + \Gamma_{\mathrm{b}}V_{\mathrm{b}} + \Gamma_{\mathrm{t}}V_{\mathrm{t}}, \tag{A.10}$$

where $YI = \int (W/s_{11})\,z^2\,\mathrm{d}z$ is the effective product of Young's modulus and area moment of inertia for the beam. It follows that the static beam deflection is governed by the usual Euler beam equation $\left(YIw''_{xx}\right)''_{xx} = q$ where q is the load force per unit length, and thus the piezoelectric effects only affect the boundary conditions of the beam.

An approximate vertical force balance at the center of mass for the proof mass affected by the external force F yields

$$m\ddot{w}_c + b\dot{w}_c + kw_c = F + \frac{\Gamma_{\mathrm{b}}}{\Lambda}V_{\mathrm{b}} + \frac{\Gamma_{\mathrm{t}}}{\Lambda}V_{\mathrm{t}}, \tag{A.11}$$

where $k = 3YI/\left[L\left(L^2 + 3L\ell + 3\ell^2\right)\right]$ is the spring constant as seen from the center of mass, which results from a steady state solution of Euler's beam equation, and b represents viscous losses in the beam–mass system. Here we have ignored the effects of a finite moment of inertia for the proof mass and the mass of the cantilever beam. The bending moments due to piezoelectric effects have been recast into effective forces acting on the center of mass by use of the length parameter Λ.

We may, with Laplace transformed quantities, write the final lumped model equations as

$$Z_m v_c = F + \frac{\Gamma_\mathrm{b}}{\Lambda} V_\mathrm{b} + \frac{\Gamma_\mathrm{t}}{\Lambda} V_\mathrm{t}, \tag{A.12}$$

$$I_\mathrm{t} = \frac{\Gamma_\mathrm{t}}{\Lambda} v_c + sC_\mathrm{t} V_\mathrm{t} \tag{A.13}$$

$$I_\mathrm{b} = \frac{\Gamma_\mathrm{b}}{\Lambda} v_c + sC_\mathrm{b} V_\mathrm{b}, \tag{A.14}$$

where v_c is the velocity of the proof mass, $Z_m = sm + b + k/s$ is the mechanical impedance of the proof mass–spring system and $s = j\omega$ is the complex frequency.

References

[1] Hudak N S and Amatucci G G 2008 Small-scale energy harvesting through thermoelectric, vibration, and radiofrequency power conversion *J. Appl. Phys.* **103** 101301

[2] Beeby S P, Tudor M J and White N M 2006 Energy harvesting vibration sources for microsystems applications *Meas. Sci. Technol.* **17** R175–95

[3] Fang H, Liu J, Xu Z, Dong L, Wang L, Chen D, Cai B and Liu Y 2006 Fabrication and performance of MEMS-based piezoelectric power generator for vibration energy harvesting *Microelectron. J.* **37** 1280–4

[4] Choi W J, Jeon Y, Jeong J H, Sood R and Kim S G 2006 Energy harvesting MEMS device based on thin film piezoelectric cantilevers *J. Electroceram.* **17** 543–8

[5] Shen D, Park J, Ajitsaria J, Choe S, Wikle H C and Kim D 2008 The design, fabrication and evaluation of a MEMS PZT cantilever with an integrated Si proof mass for vibration energy harvesting *J. Micromech. Microeng.* **18** 055017

[6] Aktakka E E, Peterson R L and Najafi K 2011 Thinned-PZT on SOI process and design optimization for piezoelectric inertial energy harvesting *Proc. Transducers (Beijing, China, June)* pp 1649–52

[7] Roundy S and Wright P K 2004 A piezoelectric vibration based generator for wireless electronics *Smart Mater. Struct.* **13** 1131–42

[8] Erturk A and Inman D J 2009 An experimentally validated bimorph cantilever model for piezoelectric energy harvesting from base excitations *Smart Mater. Struct.* **19** 025009

[9] Aktakka E E, Peterson R L and Najafi K 2011 Multi-layer PZT stacking process for piezoelectric bimorph energy harvesters *11th Int. Conf. on Micro and Nanotechnology for Power Generation and Energy Conversion Applications (Seoul, Republic of Korea, Nov.)* pp 139–42

[10] Kok S, White N M and Harris N R 2009 Fabrication and characterization of free-standing thick-film piezoelectric cantilevers for energy harvesting *Meas. Sci. Technol.* **20** 124010

[11] Xu R, Lei A, Christiansen T L, Hansen K, Guizzetti M, Birkelund K, Thomsen E V and Hansen O 2011 Screen printed PZT/PZT thick film bimorph MEMS cantilever device for vibration energy harvesting *Proc. Transducers (Beijing, China, June)* pp 679–82

[12] Xu R, Lei A, Dahl-Petersen C, Hansen K, Guizze M, Birkelund K, Thomsen E V and Hansen O 2012 Screen printed PZT/PZT thick film bimorph MEMS cantilever device for vibration energy harvesting *Sensors Actuators* A at press doi:10.1016/j.sna.2011.12.035

[13] Lei A, Xu R, Thyssen A, Stoot A C, Christiansen T L, Hansen K, Lou-Moeller R, Thomsen E V and Birkelund K 2011 MEMS-based thick film PZT vibriational energy harvester *Proc. IEEE Micro Electro Mechanical Systems (Cancun, Mexico, Jan.)* pp 125–8

[14] Hindrichsen C, Lou-Moeller R, Hansen K and Thomsen E V 2010 Advantages of PZT thick film for MEMS sensors *Sensors Actuators* A **163** 9–14

[15] Hagood N W and von Flotow A 1991 Damping of structural vibrations with piezoelectric materials and passive electrical networks *J. Sound Vib.* **146** 243–68

[16] The Institute of Electrical and Electronics Engineers 1978 *IEEE Std 1976-1978 IEEE Standard on Piezoelectricity* pp 9–14

[17] Lifshitz R and Roukes M L 2000 Thermoelastic damping in micro- and nanomechanical systems *Phys. Rev.* B **61** 5600–9

[18] Elfrink R, Kamel T M, Goedbloed M, Matova S, Hohlfeld D, van Andel Y and van Schaijk R 2009 Vibration energy harvesting with aluminum nitride-based piezoelectric devices *J. Micromech. Microeng.* **19** 094005